# Thermal nanoconversion of ferromagnetic nanoislands

O.J. Barker[1], A. Mohammadi-Motlagh[1], A. J. Wright[1], R. Batty[1], H. Finch[2], A. Vezzoli[3], P.S. Keatley*[4], and L. O'Brien*[1]

[1] Department of Physics, University of Liverpool, UK
[2] Department of Electrical Engineering and Electronics, University of Liverpool, UK
[3] Department of Chemistry, University of Liverpool, UK
[4] Department of Physics and Astronomy, University of Exeter, UK

**ABSTRACT**.

In this work, we investigate the use of post-fabrication thermal nanoconversion (TNC), using a heated scanning probe tip, to modify the magnetic properties of $Ni_{80}Fe_{20}$ elliptical nanoislands with varying aspect ratio. Despite NiFe being unoptimized for TNC, by comparing quasistatic and dynamic magneto-optical Kerr effect (MOKE) microscopy measurements, we demonstrate TNC at a contact temperature of 250°C increases the saturation magnetization of the treated nanoislands, reaching a value close to 800 kA/m. Micromagnetic simulations of the nanoislands indicate the TNC technique can be used to alter the remanent state, from single domain to vortex. These results demonstrate the opportunities afforded by TNC to modify the properties of selected areas in a thin film or patterned sample, particularly when designing magnonic crystals and other nanomagnetic devices.

*Corresponding authors: lobrien@liverpool.ac.uk and p.s.keatley@exeter.ac.uk

Standard methods for preparing masks for nanoscale pattern transfer, such as electron beam lithography, routinely allow the fabrication of designs for a wide range of applications[1 2 3 4 5]. The process is, however, typically binary in nature - a pixel in the design represents either the presence or absence of material in the layer - ultimately limiting the phase space that may be explored when developing thin film devices. The ability to change the properties of a thin film, as opposed to the physical addition or removal of material, is more challenging, particularly on a nanoscopic lengthscale, i.e., nano-conversion. Such nanoconversion, and the continuous modification of the underlying film properties, is actively sought in a variety of systems and has been demonstrated, for example, through greyscale lithography[6], chemical conversion of functional materials[7], ion implantation[8], redox of materials[9,10] and local binding of biological materials[11].

Thermal nanoconversion (TNC) is a particularly appealing approach as heat is a common route to alter the properties of a material. For example, heat is used to alter thin film magnetic properties through defect annealing, sintering, recrystallisation, demagnetization and exchange bias setting etc.[12 13 14 15 16]. An emerging approach to TNC is *via* the rastering of a heated nanoscale tip across the surface of a thin film, modifying the film in the immediate vicinity of the contact point. Such an approach to TNC has been used to great effect in magnonics and nanomagnetism to generate curved domain walls for waveguides[17], pattern spin textures[18], and the fabrication of vortex cores in crystalline films,[19] but its wider application remains underutilized.

In this work, we investigate the use of post-fabrication TNC to modify the magnetic properties of $Ni_{80}Fe_{20}$ elliptical nanoislands with varying aspect ratio (length:width). Despite $Ni_{80}Fe_{20}$ being an unoptimized material for TNC, we demonstrate that heating to $T = 280$ °C for 1 ms leads to a clear change in magnetic properties of the treated islands, consistent with ~15% increase in

Applied Physics Letters

AIP Publishing

saturation magnetization, $M_s$. Using time-resolved Kerr microscopy we evidence a change in the Kittel-like uniform-mode resonant field for TNC treated islands, suggesting $> 8\%$ increase in $M_s$ under similar TNC conditions. These results demonstrate the opportunities afforded by TNC to modify the properties of selected areas when designing magnonic crystals and other nanomagnetic devices.

To make the TNC structures, ferromagnetic nanoisland arrays, spanning 20 μm x 20 μm, were fabricated on both oxide and undoped silicon substrates using thermal scanning probe lithography (tSPL). Each array consisted of individual nanoislands, 200 nm wide with varying length $l$, either 200, 300, 400 or 800 nm, and an edge-to-edge separation of 400 nm. A schematic of the t-SPL technique is shown in Fig. 1a. A thermally sensitive bilayer resist consisting of polymethylglutarimide (PMGI; 50 nm)/polyphthalaldehyde (PPA; 30nm) is spin-coated onto the silicon oxide substrate. A heated tip is then scanned across the resist surface, and electrostatically pulled in and out of contact with the sample. The PPA layer sublimates when heated above 150 °C, transferring the pattern mask when the tip is in contact with the surface, in this case, with a write depth of ~35 nm [20]. The PMGI layer is chemically etched in a tetramethylammonium hydroxide (TMAH): isopropyl alcohol solution (1:40 by volume respectively), followed by oxygen plasma etch de-scum, exposing the substrate in the patterned regions. $Ni_{80}Fe_{20}$ is deposited through the mask *via* electron beam evaporation under ultra-high vacuum, with a thickness of 20 nm, and at a rate of 0.4 Ås$^{-1}$, source purity of 99.9% and deposition pressure $\leq 1 \times 10^{-8}$ mbar. Finally, a lift-off step using either N-methyl-2-pyrrolidone or Dimethyl Sulfoxide (DMSO) is performed to remove the remaining resist stack, leaving the nanoisland arrays seen in Fig. 1c-g.

Next, TNC was performed on a subset of the arrays, as schematically shown in Fig.1b. Neighboring, as-grown arrays which did not undergo TNC treatment provide reference samples. Heating of the arrays for TNC is performed using a scanning probe: the sample is re-aligned to the tip scan axes and the array pattern is retraced, with the tip lowered into thermal contact when positioned over the location of the patterned islands. Each $Ni_{80}Fe_{20}$ island is heated in 20 nm pixel steps, with a 1 ms tip contact time per pixel. During TNC, the scanning probe is heated with an on-tip resistive heater, maintained at a temperature, $T_H = 1000$ °C, and monitored *via* on-tip thermometer. To estimate the corresponding sample contact temperature, $T_c$, we consider a simple 1-D thermal resistance model[21]:

$$T_C = \frac{R_S}{R_T + R_C + R_S} (T_H - T_S) + T_S \qquad (1)$$

Here, $T_s = 20$ °C is the substrate temperature; $R_s, R_T$ and $R_C$ are the 1-D thermal resistances of the sample, tip and contact interface, respectively. $R_S$ was estimated to be $8.4 \times 10^7$ K/W, taking the thermal conductivity for $Ni_{80}Fe_{20}$ of 2.48 W/Km from literature [22] [23]and an island thickness of 20 nm. $R_T$ is dominated by an oxide surface layer on the silicon tip used in tSPL, with a tip resistance $R_T = 10^8$ K/W[24]. $R_C$ depends on the tip opening angle and boundary resistance, which is independent of the material in contact and takes a value of $2.0 \times 10^8$ K/W for the Silicon tips used in this work[23]. Using Eq. 1, we estimate $T_c = 240$ °C, when $T_H = 1000$ °C, for the TNC conditions applied here.

We perform spatially resolved, longitudinal geometry, magneto-optical Kerr effect (MOKE) microscopy to characterize the magnetic reversal of the TNC treated and untreated arrays. Fig 2a-d show hysteresis loops of the $x$-component of the magnetization, $M_x$, normalized to the saturation magnetization, $M_x/M_s$, *vs* applied magnetic field, $H$. The field ($\mu_0 H$) is swept at a rate of 20 mT/s.

Data are the averaged response across all islands within an array, with $l = 200$ to 800 nm shown in each panel (Fig. 2a-d, respectively). Displayed are data for the unheated (black data) and TNC heated (red data) arrays. Considering the untreated arrays first, the square hysteresis loops observed for higher aspect ratio islands ($l = 400$ and 800 nm, Figs. 2c and d) indicate sufficient shape anisotropy to ensure a single domain remanent state and sharp, domain wall-mediated reversal. The $l = 200$ and 300 nm, conversely, show the characteristic 'pinched' hysteresis loops of the magnetic vortex state[25]. Indeed, the $l = 200$ nm, circular islands show low remanence magnetization, $M_R = 0.54\,M_s$, of a flux closure or curling state. Moving to consider the TNC treated arrays, the hysteresis loops show a similar overall trend, from vortex to single domain as $l_x$ increases, however, the heated arrays remain in a flux closure or curling state up to higher aspect ratio. Indeed, sharp, single domain switching only emerges at $l = 800$ nm and a clear difference in remanence, loop area and saturation field are all visible in Figs. 2b and 2c.

The evolution from vortex state to single domain on increasing nano-island aspect ratio is a well-known micromagnetic effect observed in literature and is linked directly to the interplay between anisotropy and demagnetizing energy of the island, the latter of which is principally influenced by $M_s$ and island shape[26]. Polycrystalline $Ni_{80}Fe_{20}$ has negligible crystalline anisotropy[27], and scanning electron microscopy images of pre- and post-TNC arrays confirm the shape of the islands is unaffected by the TNC process. We therefore use micromagnetic simulations[28,29] to understand the impact of varying $M_s$ on the hysteresis loops in Fig. 2a-d. For these simulations we take the literature established values of Gilbert damping constant, $\alpha = 0.01$, and exchange constant, $A = 13 \times 10^{-12}$ m for $Ni_{80}Fe_{20}$[28].

Hysteresis loops ($M_x/M_s\ vs\ H$) generated from MuMax3 simulations of each nano-island geometry are shown in Figs. 2e-h, for varying $M_s$ from 600 kA/m (black dashed line) to that of

5

bulk $Ni_{80}Fe_{20}$, $M_s$ = 880 kA/m (yellow dashed line). The simulations show good qualitative

agreement with experimental data, with the expected evolution from vortex state to single domain

remanence on increasing nano-island aspect ratio. It is equally clear that increasing $M_s$ causes the

vortex state to be maintained up to larger aspect ratios, as might be expected given the resulting

increase in demagnetizing energy naturally favors flux closure. Figs. 2i-l show the obtained

micromagnetic equilibrium state at remanence for each $l$ value for $M_s$ = 800 kA/m. In both

experiment and modelling the reversal becomes dominated by an easy-axis response when $l$ = 800

nm for all tested cases.

At this point, we reason that the principal effect of the TNC has been to locally increase $M_s$ in

treated islands. To consider this further, and to estimate the pre- and post-treatment $M_s$ values, in

Fig. 3 we compare loop area, normalized to $M_s$ for direct comparison (Fig. 3a); change in coercive

field, normalized to the maximum value at $l$ = 800 nm (Fig. 3b); normalized remanence

[$M(H = 0)/M_s$, Fig. 3c]; and saturation field ($H_{sat}$, Fig. 3d), for experiment and numerical

simulation. Presented numerical values are averages from five repeated simulations where small

variation arises from thermal fluctuations, with error bars representing the standard error derived

from these averages. From Figs. 3a-c, we see an increase in $l_x$ increases the hysteresis loop area

as both coercivity and remanence increase, due to the expected increase in anisotropy field. The

square loop shape at large $l$ equally shows a decrease in $H_{sat}$ (Fig. 3d), since a vortex core does

not form. While there is only a minor distinction between the untreated and TNC treated arrays in

$H_c$, $H_{sat}$ or loop area, the remanent magnetization, $M_R$, shows a clear trend, particularly a

difference in the critical $l$ value above which the islands enter the single domain, high remanence

regime. Comparing the change in Fig. 3a-d, including $M_R(l)/M_s$ between heated and unheated

6

arrays, with the evolution of $M_s$ across the simulated arrays, we estimate $M_s$ increases from $\leq 700$ kA/m to >800 kA/m through TNC, representing a minimum change of 14%.

To further confirm TNC-induced changes in the magnetic properties of the treated islands, we performed spatio-temporally resolved MOKE (TR-MOKE) microscopy to acquire ferromagnetic resonance spectra from individual nanoislands. High spatial resolution was achieved using a ×100 oil immersion lens (N.A. 1.3) to focus probe laser pulses to a diffraction limited spot. The probe laser wavelength was 520 nm, derived from second harmonic generation of a 1040 nm mode-locked fibre laser with a nominal pulse duration of 140 fs and repetition rate of 80 MHz. The probe average power was attenuated to <200 µW. Global excitation of magnetization dynamics in the arrays of nanoislands was achieved by placing the sample face-up onto a 50 Ω impedance matched coplanar waveguide (CPW) with centre conductor width and ground plane separation of 0.5 mm and 0.36 mm, respectively. Nanoisland array samples were fabricated on 300 µm intrinsic Si substrates to avoid attenuation of the excitation field. A microwave current waveform from an 80 MHz comb generator, synchronized to the laser, was used to provide single frequency, phase stable excitation by narrow band pass filtering the desired excitation frequency from the output 80 MHz comb (160 MHz to 18 GHz). The output was amplified before passing through the CPW and the transmitted waveform monitored using a sampling oscilloscope. Amplitude modulation of the microwave waveform at ~31.4 kHz allowed for phase sensitive detection of the Kerr signal using a lock-in amplifier.

Time-resolved scans with ~10 ps resolution were acquired at a fixed position on an individual nanoisland for a given in-plane bias magnetic field, applied along the length of the CPW. The CPW microwave field was in-plane and perpendicular to the equilibrium magnetization, while magnetization dynamics were probed using polar MOKE to sense the out-of-plane component of

7

precession. At two time-delays, corresponding to approximately a node and antinode, the bias magnetic field was swept to acquire ferromagnetic resonance (FMR) spectra, with examples scans shown in Fig. 4b. These correspond to the real and imaginary parts of the dynamic susceptibility tensor components of the dynamic magnetization. At the resonance field and desired time delay, TR images were acquired by scanning the nanoisland arrays beneath the focused laser spot.

Fig. 4a shows an example TR-MOKE image taken of an $l = 400$ nm, $20 \times 20$ $\mu m^2$ TNC treated array, under an applied field strength of 91 mT and with a 70 ps time delay, corresponding to an antinode in the uniform precessional response of the islands. The microwave magnetic field amplitude was estimated to be ~8 kA/m for a waveform peak-to-peak voltage of ~5 V. The image confirms the resonant response of each individual island can be detected, as well as the inherent island-to-island variability in the phase and amplitude of the response. The TR-MOKE signal from FMR of an individual $l = 400$ nm island $vs$ bias magnetic field is shown in Fig. 4b. Here, the excitation frequency was 8 GHz with similar microwave field amplitude. The spectra were acquired at a fixed time delay, relative to the excitation field, either in-phase (red data, 0 ps time delay) or $\pi/2$ out-of-phase (blue data, 30 ps time delay) with the drive field. We fit both datasets, assuming a finite phase difference between drive and response, and so a contribution from both the out-of-phase precessional and in-phase dispersive response functions[30]:

$$V_i = A_i \frac{\Delta H}{4(H - H_{Res})^2 + \Delta H^2} + B_i \frac{(H - H_{Res})}{4(H - H_{Res})^2 + \Delta H^2}$$

Here, $V_i$ is the TR-MOKE signal amplitude, where $i$ is an index which represents either the in-phase or out-of-phase dataset. Both datasets are fitted, constraining the resonance field, $H_{Res}$, and peak width, $\Delta H$, between datasets to obtain a consistent estimate across both scans. From free fitting parameters $A_i$ and $B_i$ we obtain the magnitude and phase of the FMR response, however,

8

here we concern ourselves with the extracted values of $H_{Res}$ and $\Delta H$, which provide insight into changes in effective anisotropy field and damping, respectively. The FMR response was acquired from $l = 400$ nm islands, treated with different TNC anneal temperature, $T_c$, by setting different $T_H$. $H_{Res}$ was extracted through fitting the FMR fitting for different $T_H$, and is shown in Fig. 4c. The reported values represent the largest changes observed for each $T_c$, which show a clear trend of decreasing $H_{Res}$ on increasing $T_c$. From $H_{Res}$, we calculate $M_s$ assuming a Kittel-type response and taking $\gamma = 29.4$ GHz T$^{-1}$. In Fig. 4d the percentage change in $M_s$, relative to untreated islands, is plotted against $T_c$. Once again, as seen in quasistatic hysteresis loop measurements, we observe an increase in island $M_s$ under TNC treatment, with a monotonic increase found as a function of island contact temperature, $T_c$. We tentatively observe an increase in damping for TNC treated islands, however, the large uncertainty in the measured values means no statistically significant trend is found when compared with the as-grown damping value of $\alpha = 0.012 \pm 0.02$, and so we do not consider it further here.

Both quasistatic and dynamic measurements confirm an increase in $M_S$ for the islands selectively treated with TNC, with respect to $M_S$ of the control, as-deposited nanoislands. Our estimates reach $M_s \sim 800$ kA/m post-TNC, i.e., close to the room temperature value for bulk $Ni_{80}Fe_{20}$[31]. Literature examples of bulk annealing of thin $Ni_{80}Fe_{20}$ films in an inert atmosphere indicate a complex interplay between kinetics. For moderate temperatures ($T_c < 250$ °C) and short anneal times ($< 30$ mins), the process of annealing tends to increase $M_s$, due to removal of defects and modest improvement in the crystallinity of the films[32], reaching a peak of $M_s \sim 800$ kA/m at $T_c = 250$ °C. Atomic force microscopy measurements of the grain size distribution within the untreated and treated nanoislands reflects such a grain size increase, from $44.0 \pm 0.6$ nm to $49.5 \pm 1$ nm (12% increase), which is consistent with the measured increase in $M_s$. Naturally, the reasonable as-grown

9

value of $M_s \sim$ 700 kA/m in our samples limits the percentage increase achievable *via* TNC, however, the final $M_s$ achieved is in excellent agreement with that found in bulk studies[32].

Long anneal times and elevated temperatures are known to cause an increase in damping and loss of $M_s$, due to migration of Ni into the Si substrate; a natural consequence of the high diffusion constant, $D_0 = 1.7 \times 10^{-4}$ cm$^2$/s and low activation barrier, 0.15 eV, for interstitial migration within the material pairing[33]. Localized heating on short timescales is an advantage of TNC as it allows one to access different diffusion kinetics during the annealing process. Heating is highly localized, with the (typical) high thermal conductivity and large thermal mass of the substrate preventing substantial increase in $T_s$ from the localized probe. During the 1 ms anneal time, the diffusion length of Ni in Si at a temperature of 250 °C is estimated to be ~110 nm[33], more than sufficient to substantively reduce the Ni content in the ferromagnet. We thus reason that during TNC the Si substrate remains close to room temperature, circumventing Ni diffusion and preventing the decrease in $M_s$ observed in other global annealing studies[31].

To confirm this, we compare TNC treated nanoislands to samples heated in a high vacuum rapid annealer for 1 hour. To test the impact of Ni diffusion, we also consider the rapid annealing of 20 nm $Ni_{80}Fe_{20}$ nanoislands grown on a 10 nm MgO barrier layer to prevent Ni diffusion (MgO/ $Ni_{80}Fe_{20}$). Fig. 5 quantifies the change in magnetic reversal on rapid annealing to 350 °C (data are shown for the as-grown array, black data; rapid annealed data, green; annealed diffusion barrier samples, blue), where a weak increase in coercivity, and loop array is found on annealing the $MgO/Ni_{80}Fe_{20}$ nanoislands. This qualitatively mirrors increased $H_c$ and loop area following TNC treatment (Fig. 3). Comparing with samples where no diffusion barrier is present (green data), we see a stark difference: There, annealing (up to 300 °C) shows a considerable *decrease* in coercivity (up to 50%) and loop area, again indicating Ni diffusion plays a substantive role in the

magnetic response of annealed $Ni_{80}Fe_{20}$, grown on Si substrates, and that this is mitigated during the short soak times of TNC.

Finally, we turn our attention to potential surface oxidation during TNC. X-ray photoelectron spectroscopy of 300 °C annealed and unannealed $Ni_{80}Fe_{20}$ thin films confirms film oxidation in our samples proceeds by preferential Fe oxidation, with a loss of Ni and NiO observed in annealed samples, and so is limited by Fe migration to the top surface. Considering the (low) parabolic rate constant found in literature for this process, we estimate a sub-nm increase in the oxide layer for the TNC conditions applied here[34][35], again highlighting the noted robustness of $Ni_{80}Fe_{20}$ passivation and the advantages of the short anneal times achievable during TNC.

$Ni_{80}Fe_{20}$ is a common material for spintronic and magnonic devices and is used here as a demonstration for the potential of the TNC technique. However, the material is unoptimized for TNC and the reasonable as-grown $M_s$ values ($M_s \sim$ 700 kA/m) of our thin films leave only modest improvement on TNC application. Nevertheless, the ability to modify selected areas, varying the materials properties, in a pre-determined pattern offers substantial opportunity in the design of future magnetic and magnonic devices. We imagine opportunities to design 2D magnonic crystals whereby, through judicious choice of underlying material, one may tune $M_s$, anisotropy, exchange coupling or other material parameters in a continuous manner. This has already been demonstrated with exchange bias resetting in ferromagnet/antiferromagnet coupled bilayers[18] and here we show TNC annealing can directly improve $M_s$ for selected nano-islands. Despite the presented consistent trends in the optimally annealed islands, differences between dynamic and static measurements, in addition to variability in the measured change in $M_s$ in dynamic experiments for nanoislands within the same array point to potential inconsistent contact between tip and sample. Refining

contact feedback should allow precise control of this factor and remains a promising avenue of further research for those working in the field.

In conclusion, in this work we demonstrate the use of post-fabrication TNC to enhance $M_s$ in pre-patterned nanoislands, using a heated scanning probe tip. Comparing quasistatic and dynamic MOKE measurements, we determine the short anneal time and localized heating profile increases $M_s$, approaching bulk $M_s \sim 800$ kA/m at $T_c = 250$ °C. Comparing with micromagnetic simulations demonstrates that the TNC technique can be used to alter the remanent state of the islands, from single domain to vortex. These results demonstrate the opportunities afforded by TNC to modify the properties of selected areas, particularly when designing magnonic crystals and other nanomagnetic devices.

Supplementary Material

Movies of TR-MOKE image sequences acquired from an individual 300 nm × 200 nm elliptical nanoisland at different bias magnetic field showing uniform and non-uniform modes of excitation at 6 GHz.

Acknowledgements
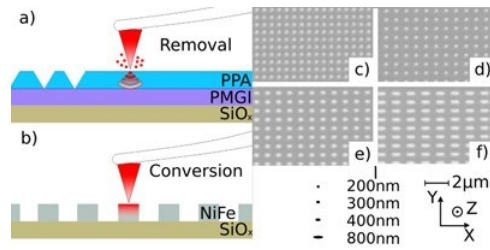
**Fig. 1.** a) Removal of material by thermomechanical sublimation during thermal scanning probe lithography. b) Thermal nanoconversion of material by local heat modification. c-g) SEM images of produced $Ni_{80}Fe_{20}$ nanoislands, where c) $l$ = 200 nm d) $l$ = 300nm e) $l$ = 400nm f) $l$ = 800nm. Inset, below (e) are the t-SPL masks for each nanoisland length, scale bar for (c-f) and coordinate system.

13
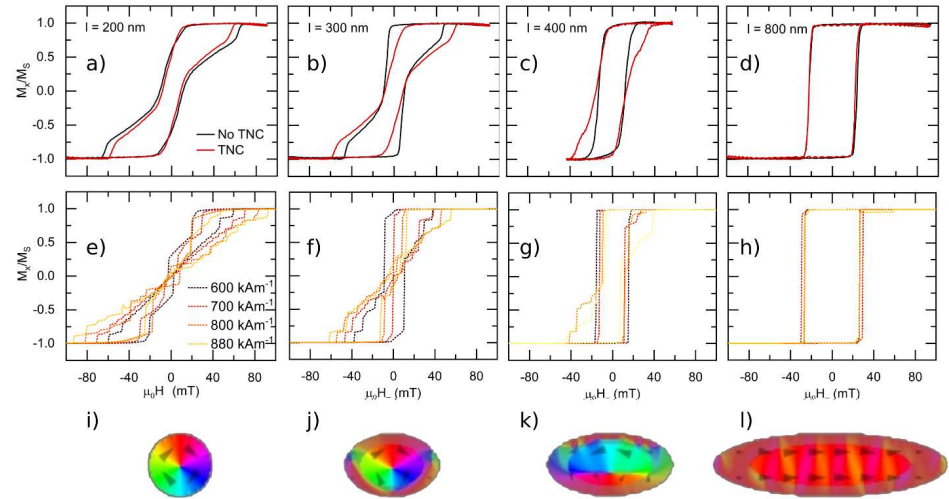
**Fig.2.** Normalized magnetization component, $M_x/M_s$, vs applied field, $\mu_0 H$, obtained from magneto-optical Kerr effect microscopy of 20 nm thick $Ni_{80}Fe_{20}$ nanoislands. Upper plots: solid lines represent longitudinal MOKE data, with $H$ applied parallel to $l$. Lower plots: dotted line shows MuMAX3 simulated response, with varying $M_s$. Images: simulated equilibrium state at remanence, where color and arrows represent in-plane magnetization direction (see vortex (i) for $M_x$ to $M_y$ color variation). a,e,i) $l = 200$ nm b,f,j) $l = 300$ nm c,g,k) $l = 400$ nm d,h,l) $l = 800$ nm.
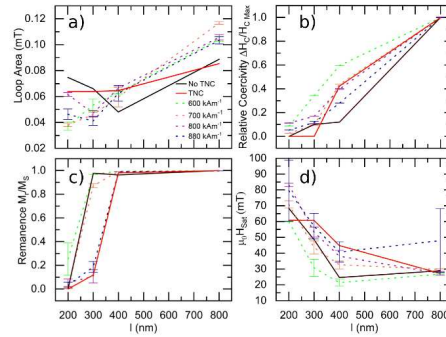
**Fig. 3.** Analysis of experimental and simulated data for varying island size, solid lines representing experimental data and dotted lines showing modelled data for different $l$. a) Area contained within the hysteresis loop, normalized by $M_s$. b) Relative change in coercivity. $H_c/H_{c\ Max}$ c) Remanent magnetization, $M_R/M_s$. d) Saturation field, $H_{Sat}$.
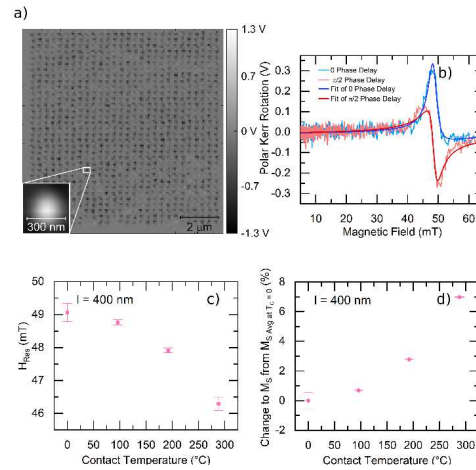
**Fig. 4.** a) Time resolved MOKE image taken of an $l = 300$ nm uniformly annealed array, taken at a field strength of 91 mT and 70 ps time delay. With insert showing high resolution reflected intensity image of a single nano-disk (white) against the substrate (black) b) Kerr effect rotation *vs* bias field under 9 GHz excitation field of a single nano-disk with signal recorded at delays of 0-1 ps (blue) and 30-31 ps (red) with fitted response. c) Extracted resonant field, $H_{Res}$, vs anneal contact temperature, $T_c$. d) Relative change in $M_s$ under TNC treatment vs contact temperature.
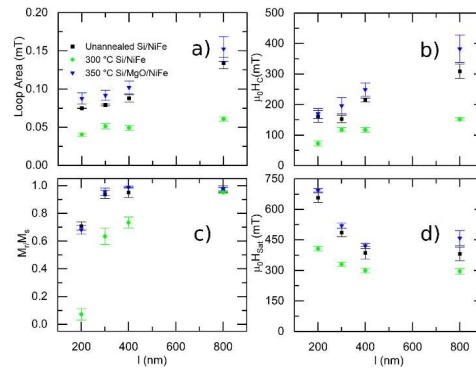
**Fig.5.** Nanoisland magnetic reversal parameters *vs* length, $l$, for as-grown $Ni_{80}Fe_{20}$ islands (black squares), annealed $Ni_{80}Fe_{20}$ islands ($T_c = 300$ °C, green squares) and annealed islands with Ni diffusion barrier $MgO/Ni_{80}Fe_{20}$ ($T_c = 350$ °C, blue triangles), obtained from longitudinal MOKE measurements. a) Area contained within the hysteresis loop, normalized by $M_s$. b) coercivity, $H_c$, c) normalized remanent magnetization, and d) saturation field, $H_{Sat}$.

## References

1      W. Srituravanich, N. Fang, C. Sun, *et al*.  Nano Letters **4**, 1085 (2004).
2      S. V. Sreenivasan,  Microsystems & Nanoengineering **3**, 17075 (2017).
3      A. Beguivin, L. O'Brien, A. Fernandez-Pacheco, *et al*.  Applied Physical Letters **101**, 062415 (2012).
4      P. Yu, J. Wu, S. Liu, *et al*.  Nano Today **11**, 704 (2016).
5      J. Ngunjiri and J. C. Garno,  Analytical Chemistry **80**, 1361 (2008).
6      G. Geng, R. Pan, C. Li, *et al*.  Laser and Photonics Reviews, **17**, 2300073 (2023).
7      D. Wouters and U. S. Schubert, Angewandte Chemie - International Edition **43**, 2480 (2004).
8      M. Kaur, S. Gautam, and N. Goyal, Materials Letters **309**, 131356 (2022).
9      R. V. Martínez, J. Martínez and R. Garcia, Nanotechnology **21**, 24530 (2010).
10     Z. Wei, D. Wang, S. Kim, *et al*,  Science **328**, 1373 (2010).
11     E. Albisetti, K. M. Carroll, X. Lu, et al. Nanotechnology **27**, 315302 (2016).
12     Y.-H. Wang, W.-C. Chen, S.-Y. Yang, *et al*.  J. Appl. Phys. **99** 08M307 (2006).
13     D. Erdem, N. S. Bingham, F. J. Heiligtag, *et al.* Adv. Funct. Mater. **26**, 1954 (2016).
14     C. Hauser, T. Richter, N. Homonnay, *et al.*,  Sci. Rep. **6**, 20827 (2016).
15     M. Albrecht and C. Brombacher, Phys. Status Solidi A, **210**, 1272 (2013).
16     T. Blachowicz and A. Ehrmann,  Coatings **11**, 122 (2021).
17     E. Albisetti, S. Tacchi, R. Silvani, *et al*.  Advanced Materials **32** 1906439 (2020).
18     E. Albisetti, D. Petti, M. Pancaldi, *et al.* Nature Nanotechnology **11**, 545 (2016).
19     H. W. Shin and J. Y. Son,  Materials Letters **213**, 331 (2018).
20     X. Liu, S. T. Howell, A. Conde-Rubio, et al. Advanced Materials **32**, 2001232 (2020).
21     F. Holzner, PhD Thesis ' Thermal scanning probe lithography using polyphthalaldehyde' ETH Zürich (2013).
22     A. Avery, S. Mason, D. Bassett et al., Physical Review B **92**, 214410 (2015).
23     B. A. Nelson, & W. P. King, Thermophysical Engineering, **12**, 98 (2008).
24     S. T. Zimmermann, D. W. R. Balkenende, A Lavrenova, et al., ACS Applied Materials & Interfaces **9**, 41454 (2017).
25     R. P. Cowburn, D. K. Koltsov, A. O. Adeyeye, et al., Physical Review Letters **83**, 1042 (1999).
26     R. P. Cowburn, Journal of Physics D: Applied Physics, **33**, R1 (2000).
27     L. F. Yin, D. H. Wei, N. Lei, et al., Physical Review Letters **97**, 067203 (2006).
28     A. Vansteenkiste, J. Leliaert, M. Dvornik et al., AIP Advances **4**, 4937 (2014).
29     L. Exl, S. Bance, F. Reichel, et al., Journal of Applied Physics **115**, 17D118 (2014).
30     Charles Kittel, *Introduction to Solid State Physics*. (2005).
31     F. Schulz, R. Lawitzki, H. Głowiński, et al., Journal of Applied Physics **129** (15), 153903 (2021).
32     Q.H. Lu, R. Huang, L.S. Wang, et al., Journal of Magnetism and Magnetic Materials **394**, 253 (2015).
33     J. Lindroos, D. P. Fenning, D. J. Backlund, et al., Journal of Applied Physics **113**, 204906 (2013).
34     W.-Y. Lee, G. Scherer, & C. R. Guarnieri, J. Electrochem. Soc. **126**, 1533 (1979).
35     M. R. Fitzsimmons, T. J. Silva, & T. M. Crawford, Physical Review B **73**, 014420 (2006).